Self-Organized Critical model of energy release in an idealized coronal loop

Laura Morales and Paul Charbonneau[1]
Département de Physique, Université de Montréal,
C.P. 6128 Succ. Centre-ville, Montréal, Qc, H3C-3J7 CANADA
laura@astro.umontreal.ca, paulchar@astro.umontreal.ca
Submitted to: *The Astrophysical Journal* - 09/27/2007

ABSTRACT

We present and discuss a new avalanche model for solar flares, based on an idealized representation of coronal loop as a bundle of magnetic flux strands wrapping around one another. The model is based on a two-dimensional cellular automaton with anisotropic connectivity, where linear ensembles of interconnected nodes define the individual strands collectively making up the coronal loop. The system is driven by random deformation of the strands, and a form of reconnection is assumed to take place when the angle subtended by two strands crossing at the same lattice site exceed some preset threshold. Driven in this manner, the cellular automaton produces avalanches of reconnection events characterized by scale-free size distributions that compare favorably with the corresponding size distribution of solar flares, as inferred observationally. Although lattice-based and highly idealized, the model satisfies the constraints $\nabla \cdot \mathbf{B} = 0$ by design, and is defined in such a way as to be readily mapped back onto coronal loops with set physical dimensions. Carrying this exercice for a generic coronal loop of length 10^{10} cm and diameter 10^{8} cm yields flare energies ranging from 10^{23} to 10^{29} erg, for a instability threshold angle of 11 degrees between contiguous magnetic flux strands. These figures square well with both observational determinations and theoretical estimates.

Subject headings: Sun: corona; Sun: flares; Self-organized criticality

---

[1]Also at Centre Observatoire du Mont Mégantic

1. Flares as avalanches

Solar flares, most spectacularly visible in the extreme ultraviolet and soft X-ray domain of the electromagnetic spectrum, are the manifestation of intermittent and impulsive release of energy in the corona. The spatial coincidence of flares with magnetic structures at the solar surface leaves no doubt that flares draw their energy from the sun's magnetic field, and their very short onset time points to magnetic reconnection as the physical mechanism responsible for extracting that energy. Systematic studies of flares from space-borne platforms have revealed the remarkable fact that the frequency distribution of solar flare energy release follows a well-defined power law, spanning eight orders of magnitude in flare energy (e.g. Dennis 1985, Aschwanden *et al.* 2000), with a logarithmic slope that is independent of the phase of the solar cycle even though the latter strongly modulates their frequency of occurrence. This is indicative of self-similarity, i.e., lack of an intrinsic scale in the flaring process, and is a particularly challenging characteristic for flare models to reproduce.

Large flares, though quite energetic, are known to be too infrequent to contribute significantly to coronal heating. The less energetic but far more numerous very small flares may however contribute significantly. E. N. Parker has championed this idea now for nearly a quarter of a century (see, e.g., Parker 1983, 1988, 1994; also Klimchuk 2006 for a general review of this and other coronal heating mechanisms). His basic point is that even if a coronal loop starts off as a modeler's dream, for example as a set of fieldlines nicely parallel to one another contained within a bent cylinder, stochastic displacement of photospheric footpoints by convective motions will inexorably distort and entangle fieldlines. Because of the high electrical conductivity of the coronal plasma, tangential discontinuities will form wherever two fieldlines are forced to bend around one another in their attempt to relax to a force-free state. The associated localized electrical currents will grow until one or more plasma instabilities set in, leading to reconnection, with concomitant plasma heating, particle acceleration, and emission of hard electromagnetic radiation. Note the energy flow here: the reservoir is the kinetic energy of convective fluid motions. Work done against magnetic tension at photospheric levels pumps energy in the form of kinks propagating upward into the coronal loop, where it becomes stored in the form of electrical current systems localized about tangential discontinuities. It is finally released as thermal energy into the corona by magnetic reconnection. Using typical values for the magnetic field strength in coronal loop and granular flow velocities, Parker (1988) estimated that the smallest reconnection event that could be produced in this manner would release some 10^{24} erg, and postulated that these "nanoflares" could account for the bulk of coronal heating.

Only one minor (and physically reasonable) addition is needed to turn Parker's

coronal heating model into an avalanche model for flare of all sizes: the assumption that reconnection at one tangential discontinuity can alter physical conditions in the vicinity of the reconnection site in a manner such that other neighboring tangential discontinuities can be pushed beyond the instability threshold; further reconnection at some of these sites can then trigger more reconnection at other sites further away from the original reconnection site, and so on along and across the loop until stability has been restored everywhere. The energy released by the ensemble of tangential discontinuities having undergone reconnection is then what we call a flare. Under this picture, there is nothing fundamentally different between a very small and a very large flare; the number of small reconnection events is just widely different.

Augmented in this way, Parker's model also contains all required ingredients for self-organized criticality (hereafter SOC; see Bak *et al.* 1987; Kadanoff *et al.* 1989; Jensen 1998; and references therein): a slowly driven (photospheric motions) open dissipative system (coronal loop) subjected to self-limiting local threshold instability (magnetic reconnection). The system is said to be "critical" because the correlation length of a perturbation is comparable to the size of the system (i.e., one small reconnection somewhere in the coronal loop can trigger reconnection along the whole loop); "self-organized" because this critical state materializes naturally following the system's own dynamics, without the need for external tuning of a control parameter. In the flare context, the SOC state is reached because photospheric fluid motions inexorably entangle the magnetic fieldines within the coronal loop, building up more and more tangential discontinuities until the instability threshold is exceeded somewhere. The exact form of the fluid motions does not matter, as long as they displace the footpoints on a timescale much longer than the readjustment time of the magnetic field within the loop.

This idea of flares as avalanches of reconnection events was first embodied into a working model by Lu & Hamilton 1991 (hereafter LH91), but see also Zirker & Cleveland (1993). Following the seminal work of Bak, Tang & Wiesenfeld (1987) on self-organized criticality in sandpile models, they designed a cellular automaton where a quantity B_k related to the magnetic field is defined on every node k of a computational grid. Small increments δB are then added in succession at randomly chosen nodes on the grid. A node is deemed to become unstable if the quantity

$$Z_k = \left| B_k - \frac{1}{n} \sum_n B_n \right| \ , \tag{1}$$

where the sum runs over node k's n nearest neighbors on the lattice, exceeds a pre-set

threshold value Z_c[2]. Whenever this happens, the nodal field B_k is redistributed according to the following discrete rules, which are the model's analog of reconnection:

$$B_k \rightarrow B_k - \frac{6}{7} Z_k \ , \qquad B_n \rightarrow B_n + \frac{1}{7} Z_k \ , \tag{2}$$

where the index n runs over the same nearest neighbors nodes involved in eq. (1), and the numerical factors pertain to a 3D cartesian grid with six nearest neighbors per interior node. These rules conserve the magnitude of B, but lead to a decrease in B^2 summed over the nodes involved in the redistribution, which is taken to represent energy liberated by magnetic reconnection, and is the model's equivalent of a Parker nanoflare. But the crucial aspect is that this redistribution can also push one of the nearest neighbor node over the stability threshold, triggering further redistribution events, and so on across the lattice until every node is once again satisfying the stability criterion. Flares are then associated with these avalanche of redistribution events, and again here the distinction between large and small flares is simply the number of nodes involved in the avalanche. Lu & Hamilton (1991; see also Lu *et al.* 1993, hereafter LHMB) showed that this very simple model naturally produces robust power laws in the frequency distributions of flare energy release, peak amplitude, and duration, with logarithmic slopes in fairly good agreement with observationally-inferred values (see Charbonneau *et al.* 2001 for a review of this and related SOC models of solar flares). To go beyond flare statistics, however, one needs to assign physical meaning to the nodal variable. This is where things rapidly become tricky. The obvious identification of the nodal variable is with the coronal magnetic field $\mathbf{B}$, in which case $\sum \mathbf{B}_k^2$ is indeed a magnetic energy. However the driving process is such that over the lattice, $\nabla \cdot \mathbf{B} \neq 0$ in general, which is physically unsatisfactory. LHMB proposed an alternate identification of the nodal field with a magnetic vector potential $\mathbf{A}$, where the magnetic field $\mathbf{B} = \nabla \times \mathbf{A}$. The solenoidal constraint $\nabla \cdot \mathbf{B} = 0$ is now satisfied identically, and adding a nodal increment $\delta\mathbf{A}$ becomes akin to adding some twist somewhere in the coronal loop, which is in line with Parker's picture of forcing via footpoint motions. The stability measure (1) is now expressed in terms of the Laplacian of $\mathbf{A}$, which in turn is directly related to the magnitude of the electrical current density $\mathbf{J}$ under the pre-Maxwellian form of Ampere's Law:

$$\nabla \times \mathbf{B} = -\nabla^2 \mathbf{A} = \frac{4\pi}{c} \mathbf{J} \ , \tag{3}$$

under the Coulomb gauge $\nabla \cdot \mathbf{A} = \mathbf{0}$. However, the lattice sum $\sum \mathbf{A}_k^2$ is now no longer a magnetic energy. Isliker *et al.* (2000, 2001) have shown, in the context of a specific

[2]Note that on a regular Cartesian grid, eq.(1) is equivalent to a second-order centered finite difference discretization of a Laplacian operator acting on the nodal field.

sandpile model, that variations of this quantity during a large avalanche do correlate, albeit statistically, with variations in $\sum(\nabla \times \mathbf{A})^2$. Unfortunately, the corresponding magnetic field configurations are not particularly solar-like.

Another important interpretive issue in the flare context is the underlying physical nature of the stability criterion and redistribution rules. The fundamentally discrete nature of the sandpile model places it a long way from the modeling framework most commonly used in the flare context, namely magnetohydrodynamics. Aware of this fact, Lu (1995) demonstrated that a driven 1D nonlinear diffusion equation can lead to SOC and power-law in dissipated energies. Partial differential equations have also been obtained by reverse engineering of the various cellular automaton rules used in SOC models of solar flares (Isliker *et al.* 1998; Charbonneau *et al.* 2001, §4). In particular, Liu *et al.* (2002) obtained in this manner a nonlinear hyperdiffusion equation from a 1D sandpile model *à la* Lu & Hamilton. They went on to extract critical exponents by a renormalization analysis, and found that the numerical values of these exponents compared favorably to those inferred empirically from running the discrete sandpile model. More recently Bélanger *et al.* (2007) have repeated Lu (1995)'s computational experiment, but using a 2D version of Liu *et al.*'s nonlinear hyperdiffusion equation, and found avalanching behavior comparing very well with the corresponding discrete 2D model. The upshot of all this is that the discrete CA rules of sandpile models, as *ad hoc* as they may appear, are in fact mimicking a physical process with a known and sound physical pedigree, namely diffusion. Whether or not the aforementioned reverse-engineered partial differential equations should be considered superior to the original discrete cellular automaton is a question in epistemology, and one far from uninteresting at that. The fact remains that these nonlinear hyperdiffusions equations are not related to the usual partial differential equations of magnetohydrodynamics in any obvious way, which leaves their physical interpretation essentially as open as that of the discrete CA model from which they were obtained.

In this paper we adopt the alternate approach of designing an avalanche model that, right from the beginning, follows Parker's physical picture much more closely than the now-classical SOC sandpile models of the type introduced by Lu & Hamilton. The idea is to use magnetic fieldlines as basic dynamical elements, which guarantees $\nabla \cdot \mathbf{B} = 0$. Starting with a set of parallel fieldlines of uniform strength defining a "coronal loop", we drive the system by introducing successive, discrete local deformations, which leads to tangential discontinuities where fieldlines "cross" , and use the angle subtended by the two fieldlines at the crossing points as a criterion for stability. When instability occurs, we reconnect fieldlines, thus restoring stability, altering topology, and releasing magnetic energy. The model remains a form of cellular automaton, since the driving and redistribution are both introduced as simple, discrete rules for modifying the shape and connectivity of fieldlines.

Section 2 describes the various ingredient of our cellular automaton model, focusing in particular on the redistribution rules introduced to mimic magnetic reconnection. Representative simulation results are presented in §3, where we examine both the evolution towards the SOC state, as well as statistical properties of flares/avalanches in the SOC state. Section 4 comes back to physical considerations in the solar flare context, including rescaling of the energy release in the model in terms of physical units. We conclude in §5 by summarizing our most important results, identifying aspects of the model open for further improvement, and outlining the road ahead towards more physically accurate modelling of solar flares in the SOC context.

2. The cellular automaton

As with other SOC avalanche models, definition of the cellular automaton requires that one specifies a lattice structure, a driving mechanism, a stability criterion and a set of redistribution rules. In the flare context one also needs to assign a magnetic energy to any state of the lattice, and compute the energy liberated by avalanches of redistribution events. We consider each of these model components in turn.

2.1. The lattice

The system consists of a $2\,D$ lattice of size $N \times N$ that (initially) forms a network of equally spaced vertically interconnected nodes, with periodic boundary conditions in the horizontal direction. We assume that each vertical line so defined represents a magnetic flux strand (or tube), i.e., a bundle of magnetic fieldlines behaving as a coherent entity. Figure 1 shows an example of a 6×6 lattice, where two nodes have been displaced from their starting position (more shortly on nodal displacements). The lattice can be thought as the external surface of a 'straightened' coronal loop made of close-packed magnetic flux strands, with the upper and lower boundaries corresponding to the photosphere. For the time being, in keeping with cellular automaton tradition, the vertical and horizontal internodal distances are taken to be the same, and define our length unit. The lattice can easily be rescaled *a posteriori* to a pseudo-loop of length much longer than its diameter for the purpose of physical analysis, as will be done in §4 below.

We label each node using a vectorial index $\mathbf{k} = (i, j)$, where the index i labels a magnetic flux strand and the index k the position along the i^{th} strand. Initially each set of vertically interconnected nodes defines a flux strand of dimensionless length $l_i(0) = N - 1$.

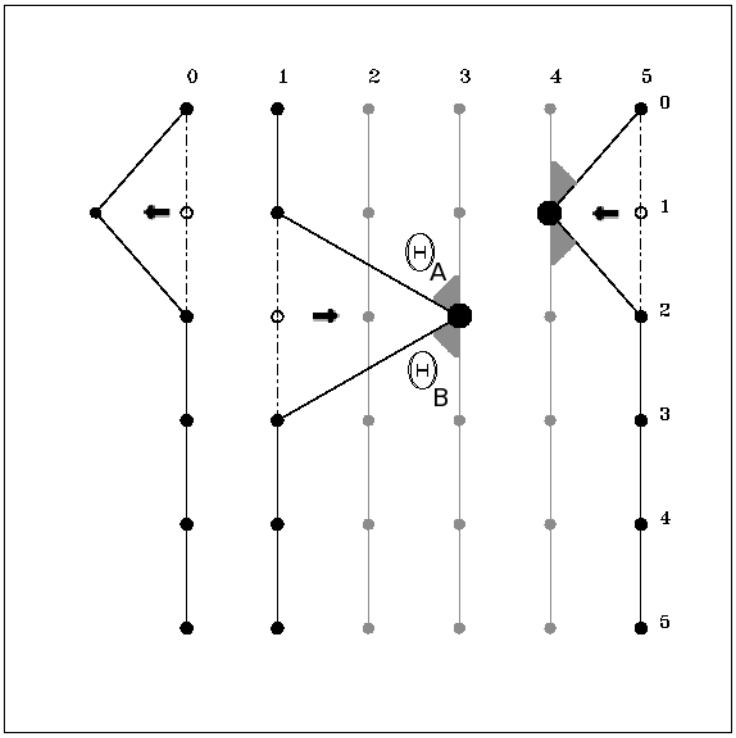

Fig. 1.— Detail of a small lattice showing the basic lattice structure and driving mechanism. Strands are numbered from left to right and nodes along a given strand, from top to botton. Here for strand 1 the node $(1, 2)$ has been displaced two units to the right. Periodic boundary conditions are enforced, so that strands 0 and 5 always experience the same displacement (here one unit to the left for node $(5, 1)$). The gray shaded region indicates that two angles formed where two flux strands meet at the same lattice site. The first is between strands 4 and 5: $\Theta_{[4,1]} = \frac{\pi}{2}$ and the one formed between strands 1 and 3 is $\Theta_{[3,2]} \sim 2.21$. Here and in all similar figures to follow, open circles indicate lattice sites currently unoccupied by a node.

It will prove important to distinguish, in what follows, between a node (identifying a position along a strand) and a lattice site, i.e., a pair of discrete $[x, y]$ cartesian coordinates; the latter will be denoted by square brackets.

Because the lattice is horizontally periodic, the first and last flux strands are one and the same; we label the first flux strand $i = 0$ to emphasize that it is not an independent entity. Note also that the lattice connectivity is here strongly anisotropic, with only top+down connectivity, unlike the top+down+right+left in 2D classical cellular automaton of the Lu & Hamilton variety (see Fig. 1 in Charbonneau *et al.* 2001).

2.2. Lattice energy

We need to define a measure of the magnetic energy stored in the lattice at any given iteration. The total magnetic energy within a volume V is:

$$E_B = \frac{1}{8\pi} \int_V \mathbf{B}^2 \mathrm{d}V \ . \tag{4}$$

We begin by establishing a relation between the length of each flux strand and its magnetic field strength. The mass contained within a cylindrical flux strand of length l, cross-section A and constant density ρ is: $M = \rho\, A\, l$. If the flux strand behaves as a coherent entity, then upon stretching to a length l', its cross-section will shrink to A' so as to satisfy the mass conservation constraint $A\, l = A'\, l'$ in an incompressible fluid. On the other hand, conservation of magnetic flux also imposes a relation between the magnetic field strength and the cross-section: $B\, A = B'\, A'$, for a vertically-oriented, constant magnetic field within the strand. From these two conservation laws we obtain the intensity of the new magnetic field B' in terms of the length the flux strands: $B' = B \times (l'/l)$.

In terms of this model representation of the coronal loop, eq. (4) becomes

$$E(t) = l_0\, A_0\, B_0^2 \sum_{i=1}^{N-1} l_i^2(t), \tag{5}$$

where l_0, A_0 and B_0 are the initial length, cross-section and field strength of the strands, and $l_i(t)$ is the length of strand i at time t. Since a flux strand is "discretized" into N nodes (including boundary nodes), it has an initial length $l_0 \propto N - 1$; further assuming that in the initial state the flux strands are space-filling, the initial energy of a $N \times N$ lattice will be:

$$E_0 = l_0\, A_0\, B_0^2\, (N-1)^3 \tag{6}$$

This quantity will be used as our unit of energy in all that follows.

2.3. Driving mechanism

We now need a driving mechanism to inject energy into the lattice. This is achieved by introducing, at each (non-avalanching) iteration horizontal displacements of a randomly chosen single node. Displacement towards the right is referred to as positive (δ_+), and to the right as negative (δ_-). For example, on Figure 1 the set of nodes $\{(1,0),(1,1),(1,2),(1,3),(1,4),(1,5)\}$ still defines flux strand number 1, after node $(1,2)$ was displaced two units to its right.
We set $\delta_+ = 2$ and $\delta_- = 1$, with equal probability for each choice at any node and iteration. Each node then ends up executing, over a great many iteration, a biased 1D random walk. The choice $\delta_+ > \delta_-$ is arbitrary, but an inequality is needed for the flux strands to develop a global pattern of twist as the simulation proceeds. This will also lead, statistically, to a gradual lenghtening of each flux strand, so that the lattice energy goes up, as per eq. (5), following the introduction of these nodal displacements. Evidently more complicated schemes on the same theme could be devised, but this very simple one was found to succesfully drive the system to a SOC state, as demonstrated shortly.

Note that in the initial state, all lattice sites are occuppied by a single node belonging to a single vertical flux strand. As driving proceeds, however, some lattice sites can become empty, such as site $[1,2]$ on Fig. 1 (open circle), or be occuppied by more than one node, such as site $[3,2]$, occuppied by nodes $(1,2)$ and $(3,2)$, or site $[4,1]$, occuppied by nodes $(4,1)$ and $(5,1)$.

Consider now any horizontal plane, equivalent to a cross-section of the loop. The nature of our driving mechanism is such that the number of flux strands crossing that plane is always $N-1$. Moreover, our adopted procedure to vary the strength of a flux strand in response to variations in its length conserves magnetic flux within the strand by design. This implies that our model automatically satisfies the flux conservation constraint $\nabla \cdot \mathbf{B} = 0$ globally as well.

As with most conventional SOC model, driving only takes place when the lattice is everywhere stable (i.e., no avalanches). In the solar flare context this is a good approximation, given that driving is associated with photospheric fluid motions (with characteristic timescale of some tens of minutes for the granular flow), while avalanching is associated with magnetic reconnection and characteristic timescale below a few minutes. Nodes at the upper and lower boundaries are excluded from the driving process, again in order to favor the buildup of a global twist pattern along our pseudo-loop.

2.4. Stability criterion

Each node in the lattice now has to be tested for stability. Parker (1983) argues that whenever two misaligned flux strands are pressed together, a tangential discontinuity forms, with which is associated an electrical current sheet. Reconnection takes place if the current magnitude exceeds some threshold, which translates into a critical angle subtended by the magnetic fieldlines forming the outer flux surfaces of each flux tube (see also Parker 1988). The evolution of such a flux strand configuration has been simulated recently by Dahlburg *et al.* (2005), who confirm Parker's general scenario, although they trace the onset of fast reconnection to a secondary instability of the current sheet.

This overall scenario is readily representable in our model, by using the angle subtended by two flux strands crossing at the same lattice site as a criterion for instability. We define the total angle $\Theta_{[i,j]}$ formed between two strands as the sum between the angle formed with respect to the vertical direction by the two strands that "enter" site $[i, j]$ from above and the two strands that "leave" the site towards the bottom. On Figure 1 for example, strands number 1 and 3 meet at site $[3, 2]$. In this case both angles (Θ_A and Θ_B) are the same: $\Theta_A = \Theta_B = \arctan[\frac{|1-3|}{|2-1|}] = 1.107\,\mathrm{rad}$, where the numerator of the fraction is obtained by the difference between the first component of the upper node (in this case 1) and the first component of the site where the angle is being formed (in this case 3). On the other hand the denominator of the fraction will always be equal to 1 because it always corresponds to a single vertical increment (internodal distance) along each strand. This gives a total angle of $\Theta_{[3,2]} = 2\arctan(2) = 2.214\,\mathrm{rad}$. We then assume that the site is unstable whenever this total angle is greater than some preset threshold value Θ_c. If it was the case that $\Theta_c = 2\,\mathrm{rad}$, then here the site [3,2] is unstable and we need to introduce a redistribution rule.

2.5. Redistribution rules

If any one lattice site has been found to be unstable, a redistribution process is needed to restore stability. This can be achieved either by reducing the angle subtented by flux strands crossing at the unstable site[3], or displacing the offending node from one of the flux strands away from the site, thus "eliminating" the unstable angle. Whichever occurs, an important additional constraint is that the redistribution must release magnetic energy

[3]Of course, real vector magnetic fields do not "cross" (null points notwithstanding), as this would imply that **B** is no longer a single-valued function at the crossing point. Crossings on our 2D lattice are simply the analogue of Parker's tangential discontinuities.

(otherwise it could not be mimicking a "spontaneously" occurring magnetic instability).

For illustrative purposes, consider the situation shown on Fig. 2A, again for an exceedingly small 6×6 lattice. Following a positive displacement of node $(1, 3)$ by two units, strands 1 and 3 now cross at site $[3, 3]$ with a total angle $\Theta_{[3,3]} = 2.21$; for a threshold $\Theta_c = 2$, this angle is deemed unstable (indicated by a bigger black dot). The reconnection procedure begins with the reconnection of strands 1 and 3, by a cut-and-splice operation at site $[3, 3]$ (A→B on Fig. 2B). After this procedure node $(3, 3)$ is displaced from the unstable site $[3, 3]$ to site $[2, 3]$ (B→C). Site $[3, 3]$ is now trivially stable since it is only occuppied by strand 1, but strand 3 now crosses strand 2 at site $[2, 3]$. The total angle formed there is $\Theta_{[2,3]} = \pi/2$, and is here stable for $\Theta_c = 2$.

At this point we check whether energy has been released: if the energy of the new configuration is smaller than the energy of the previous configuration the two-step redistribution scheme is considered complete, and the simulation can go on to the following iteration. However, the relocation of one of the nodes may have now produced a new unstable angle at a neigbouring site; if so redistribution begins anew, and so on in classical avalanching manner.

If the "two-step" redistribution scheme of Fig. 2 has not been succesful, in the sense that it would lead to an *increase* of lattice energy, then we have to introduce an additional step. To do this we operate over the four nearest nodal neighbors of the unstable site, i.e., nodes located at $j \pm 1$ on each of the two strands crossing at the unstable site. One at a time, each of these nodal neighbours is displaced randomly right or left, and the (provisional) lattice energy recomputed and compared to the current lattice energy. The procedure stops as soon as one such energy-reducing displacement is found. We call this procedure a "three-step" redistribution scheme. An example is shown in Figure 3. Here the total angle $\Theta_{[3,2]} = \Theta_A + \Theta_B + \Theta_D$ is comprised of three contributions, namely $\Theta_A = \Theta_D = \arctan(1) = \pi/4$, and $\Theta_D = \arctan(2) \sim 1.10$, so that $\Theta_{[3,2]} = 2.67$. Assuming once again that $\Theta_c = 2$, then $[3, 2]$ is an unstable site. We begin redistribution in the same manner as before: strands 2 and 3 are reconnected (A→ B), but at site $[3, 2]$ we still have not reduced or eliminated the unstable angle; moreover, the lattice energy has risen from $1.32E_0$. to $1.332E_0$. Either one (randomly chosen) of the two nodes occupying that site is then displaced. In this case the node $(3, 2)$ (belonging to strand number 3) was moved one unit to its left (B→C). In this manner the site $[3, 2]$ is no longer unstable, but lattice energy has now climbed to $1.4E_0$. With lattice energy having increased throughout the A→C sequence, it becomes necessary to add an additional step to the redistribution scheme. This new step consists in moving one of the four neigbouring node (one at a time) and monitor the corresponding variations in lattice energy. Here the four neigbouring nodes are at sites:

$[2,1]$, $[5,1]$, $[2,3]$ and $[3,3]$ (open squares). The order in which these neighbouring nodes are displaced, and the direction of the horizontal displacement, are both chosen randomly. For the specific case illustrated in Fig. 3, node $(3,1)$ is displaced from site $[5,1]$ to $[4,1]$ (C→D), and this turned out to to lower the lattice energy to $1.19E_0$, so that the total energy released during the redistribution is $E_r = E_A - E_D = 0.13E_0$. This brings the three-step scheme redistribution scheme to a close. However, this final configuration D now contains a new unstable site at $[4,1]$. This is the beginning of an avalanche.

Whether the two- or three-step redistribution scheme ends up being used, all operations are assumed to take place within a single time iteration. Monitoring of our model runs reveals that the three-steps redistribution scheme ends up taking place at 40% to 45% of unstable nodes (depending on lattice site and threshold angle), with the remainder redistributing according to the basic 2-steps algorithm. Whichever version of the redistribution scheme ends up being used, the sum of all energy so released at each unstable site represents the energy released by the flare at that iteration.

The reconnection step in our redistribution schemes (A → B on Fig. 2) may appear superfluous, as it is not changing anything to the distribution of angles at or near the unstable site, nor is it changing the total length of the two strands involved. It is, however, changing the lattice energy (proportional to the sum of the lengths squared, viz. eq. 5). Its most important role, however, is to allow topological changes in the lattice; otherwise the simulation rapidly reaches a stationary state characterized by very frequent small avalanches, where nodes just move back and forth in response to driving and redistribution, with all strands arched to the right (for $\delta_+ > \delta_-$) with similar curvatures. There is a direct analogy here with Parker's nanoflare scenario, where reconnection is needed to break the topological constraints imposed by flux-freezing, with energy release being a form of side-effect associated with the return of the stressed coronal loop to a metastable dynamical equilibrium.

3. Model Results

We have run the cellular automaton described in the preceeding section for different lattice sizes and stability threshold values, as listed in Table 1. In all cases driving makes uses of an anisotropic perturbation amplitude, i.e., $\delta_+ = 2$ and $\delta_- = 1$, chosen randomly but with equal probability at each driving iteration. All simulation begin with a configuration of vertically-oriented, straight flux strands parallel to one another.

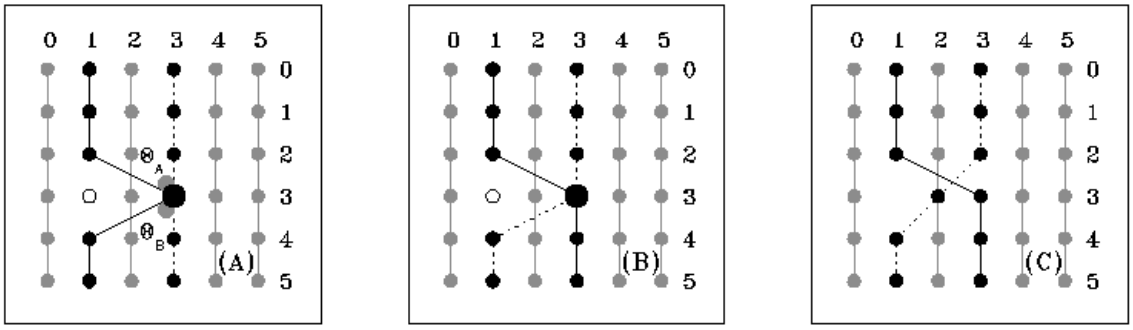

Fig. 2.— A sequence of the two-step redistribution scheme. In figure (A) we can identify the unstable site $[3,3]$ (larger black dot) formed by flux strands 1 and 3. The total energy at this stage is: $E_A = 1.25\,E_0$. In figure (B) strands are reconnected. This procedure is successful in reducing the total energy ($E_B = 1.22\,E_0$) but the site remains unstable. In (C) the node $(3,3)$, that belongs to strand 1, is displaced (to the left) leading to a configuration where the total energy is $E_C = 1.18\,E_0$ and the unstable angle is eliminated. The energy released by the whole procedure is $E_r = E_A - E_C = 0.07\,E_0$.

Table 1: Simulations parameters and global results

Simulation	N	Θ_c(rad)	η	$\langle\eta\rangle$	$t_{SOC}[10^5]$
A1	32	2	1.45	0.00280	5
A2	32	2.25	1.56	0.00253	5.9
A3	32	2.5	1.33	0.00195	7.5
B1	64	2	0.62	0.00091	2
B2	64	2.25	0.72	0.00060	3.2
B3	64	2.5	0.21	0.00040	5
C1	128	2	0.13	0.00072	2.8
C2	128	2.25	0.04	0.00052	3.3
C3	128	2.5	0.15	0.00034	8

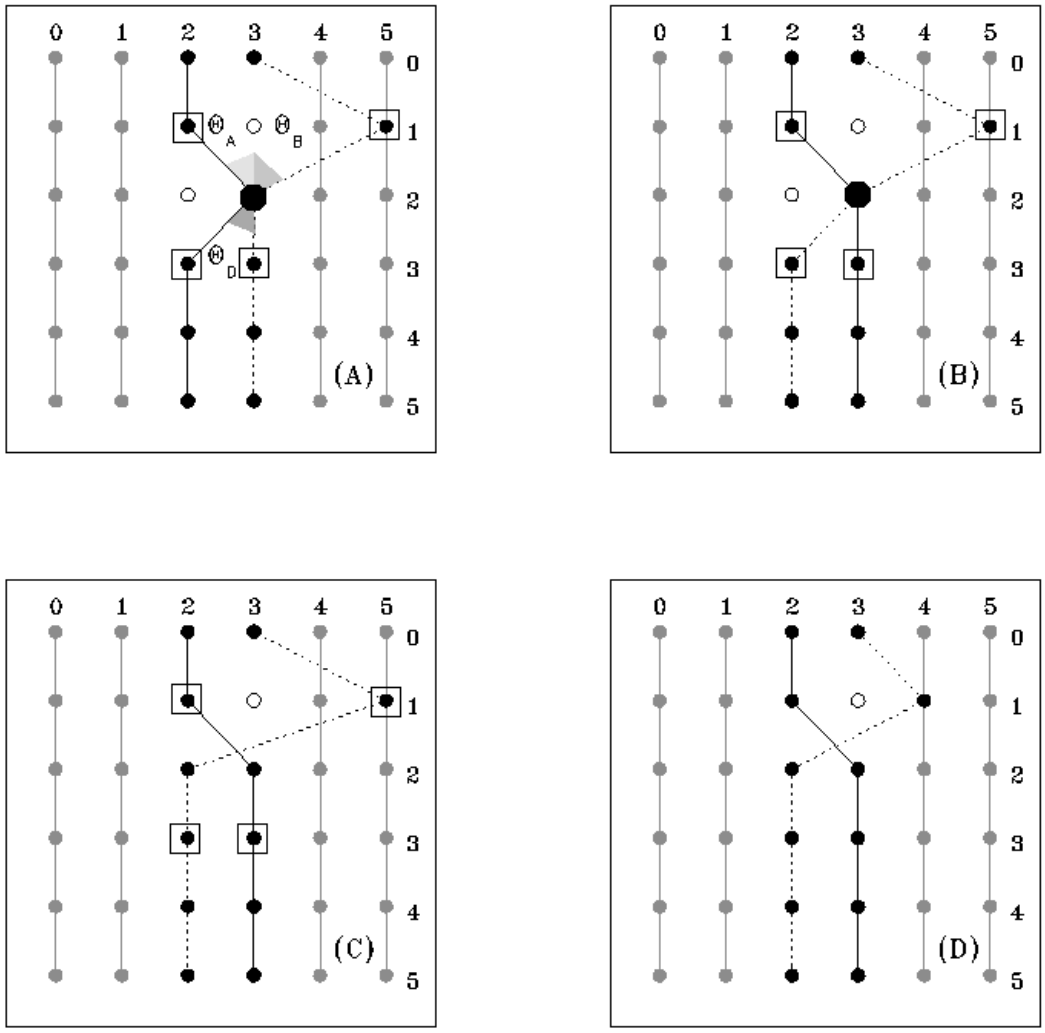

Fig. 3.— An example of the three-steps redistribution scheme applied when the two-steps scheme fails to release energy. In (A) strands 2 and 3 form an unstable angle at site $[3,2]$ (larger black dot): $\Theta_{[3,2]} = \Theta_A + \Theta_B + \Theta_D$, as labeled. The lattice energy is here equal to $1.32E_0$. Panel (B) shows the lattice after the reconnection step; the new lattice energy is $1.332E_0$, but the site $[3,2]$ remains unstable. Panel (C) shows configuration after displacing one node at the unstable site, with lattice energy $E_C = 1.4E_0$ and panel (D) the configuration resulting from the displacement of one of the four nearest-nodal neighbours (open squares), finally lowering the lattice energy to $E_D = 1.19E_0$. Here the three-steps sequence A→B→C→D has released an amount of energy equal to $E_r = E_A - E_D = 0.13E_0$.

3.1. Getting to the SOC state

Figure 4 shows results for the first 1.5×10^6 iterations of simulation C2 (128×128 lattice, $\Theta_c = 2.5$), and is representative of other runs at different stability thresholds or lattice sizes. Part (A) shows the variation of lattice energy (solid line), part (B) the energy released by avalanches, and part (C) the frequency distribution of flux strand lengths at four (non-avalanching) iterations, corresponding to times indicated by solid dots and labeled *a* through *d* on part (A).

As flux strands are inexorably stretched by the driving process, the lattice energy grows rather quickly at first, increasing by a factor of ~ 6 with respect to the initial energy. During this growth phase the mean of the distribution of strands lengths (Fig. 4C) increases more than twofold, while the distribution itself broadens significantly. The lattice energy levels off gradually after some $\simeq 3 \times 10^5$ iterations, while small avalanches take place intermittently. By then a statistically stationary state seems to have been reached, but pushing the simulation further reveals a rather sudden increase in the size of the largest avalanches, taking place here after some $\simeq 9 \times 10^5$ iterations, and accompanied by a small but significant drop in lattice energy. It is only now that the system is in a truly stationary state, which we identify as a SOC state. As in the Lu & Hamilton model, arrival at the SOC state is accompanied by a sudden increase in the size of the largest avalanches (compare Fig. 4 herein to Fig. 3 in Charbonneau *et al.* 2001). In the context of the present model, the best indicator we have found to ascertain when this occurs is the mean rate of energy released by avalanches, plotted along the bottom of Fig. 4(A) as a gray line, which rises abruptly upon arrival in the SOC state. Somewhat surprisingly, one notes on part (C) that the distributions of flux strand lengths do not show large differences between snapshots *c* and *d*, except perhaps for the distribution in the SOC state being a little broader. It's not so much the length of the strands that matters, but the pattern of crossing angles they make on the lattice. The time at which the SOC state appears is henceforth denoted t_{SOC}, and is listed in in table 1 for all simulations included therein. Examination of the various simulation runs reveals that it is only starting at t_{SOC} that avalanche spanning the whole lattice begin to take place.

3.2. Avalanche energetics

In the SOC state, the amount of energy released by the larger avalanches is one to two orders of magnitude smaller than the total lattice energy. Releasing a few percent of the lattice energy is still quite substantial; for example, in the 2D version of the Lu & Hamilton model run on a lattice of comparable size, that fraction is around 10^{-6}. In order

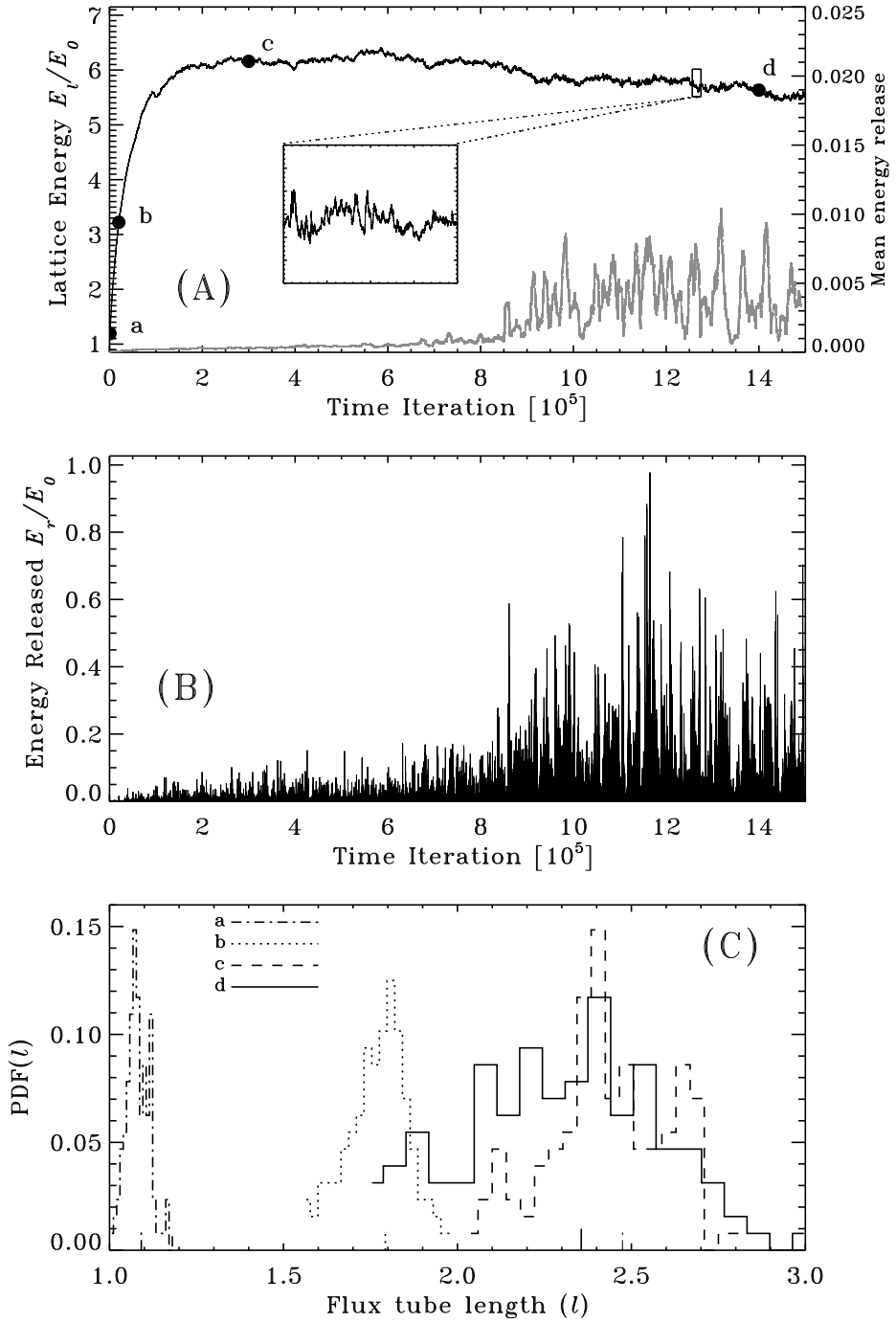

Fig. 4.— Time series of (A) total lattice energy and (B) energy released in avalanches for a 128×128 node lattice with $\Theta_c = 2.5$ rad. The inset on panel A shows a small portion of the lattice energy time series within the SOC, and the gray line shows the mean value of energy release calculated as a running mean spanning one thousand iterations. Panel (C) depicts the frequency distribution of strand length values extracted at the four different epochs in the simulation indicated by the solid dots along the energy release curve on part A.

to quantify the efficiency of our cellular automaton we define a ratio (η) between the energy liberated by the largest avalanche to the mean lattice energy in the SOC state, as well as a ratio ($\langle\eta\rangle$) of mean energy release per iteration to the mean lattice energy. Both of these quantities are listed in table 1. For any fixed lattice size, the ratio $\langle\eta\rangle$ is found to decrease as the critical threshold angle is increased. This trend is precisely that suggested by the theoretical analysis presented in Parker (1988).

Figure 5 shows three histograms of the frequency distribution of angles normalized to the instability threshold Θ_c. The distributions are constructed using forty non-avalanching iterations, widely spaced in time but all at times larger than $t_{\rm SOC}$, in simulations A2, A3 and C3 (see Table 1), as labeled. In view of the discrete nature of the nodal distribution along flux strands and of the nodal displacements used for driving, the geometrically realizable angles at lattice sites are themselves not uniformly distributed in the $[0, \pi]$ interval, which is why in part the binned distributions of unstable angles on Fig. 5 show so much structure. Nonetheless, all distributions are similarly shaped and have a mean value $\Theta/\Theta_c \sim 0.6$, for varying threshold angles and lattice sizes. Moreover, in all cases the vast majority of angles formed at sites where two strands cross are well below their stability threshold. This is analogous to the Lu & Hamilton model, where the majority of lattice nodes also present a curvature significantly below the curvature threshold (see Fig. 4 in Charbonneau *et al.* 2001).

3.3. Spatial structure of avalanches

Figure 6 illustrates the unfolding of a typical large avalanche in the B1 simulation after the SOC state has been reached. The first five frames (A through E) are snapshots showing the locii of unstable sites at specific iterations in the course the avalanche, with (A) corresponding to onset (a first, single unstable site), (C) to the iteration with peak energy release, and (E) to the end of the avalanche, here with a single remaining unstable site. On frames (A) and (E) the global shape of the two flux strands crossing at the unstable site are also plotted. Frame (F) shows the "footprint" of the avalanche, i.e., the locii of all lattice sites having gone unstable at least once during the avalanche, here adding up to 204 sites. Note the small "island" of unstable sites to the right of the main avalanche footprint. This may appear odd —and has no counterpart in classical cellular automaton such as the LHMB model,— but recall that here the nearest neighbour nodes of a node at an unstable site $[i, j]$ need not be located only at $[i \pm 1, j \pm 1]$; On Fig. 1 for example, node $(1, 2)$ located at site $[3, 2]$ has its two nearest neighbour top+down nodes at sites $[1, 1]$ and $[1, 3]$). What matter in our model are nearest neighbours along a given flux strand, which

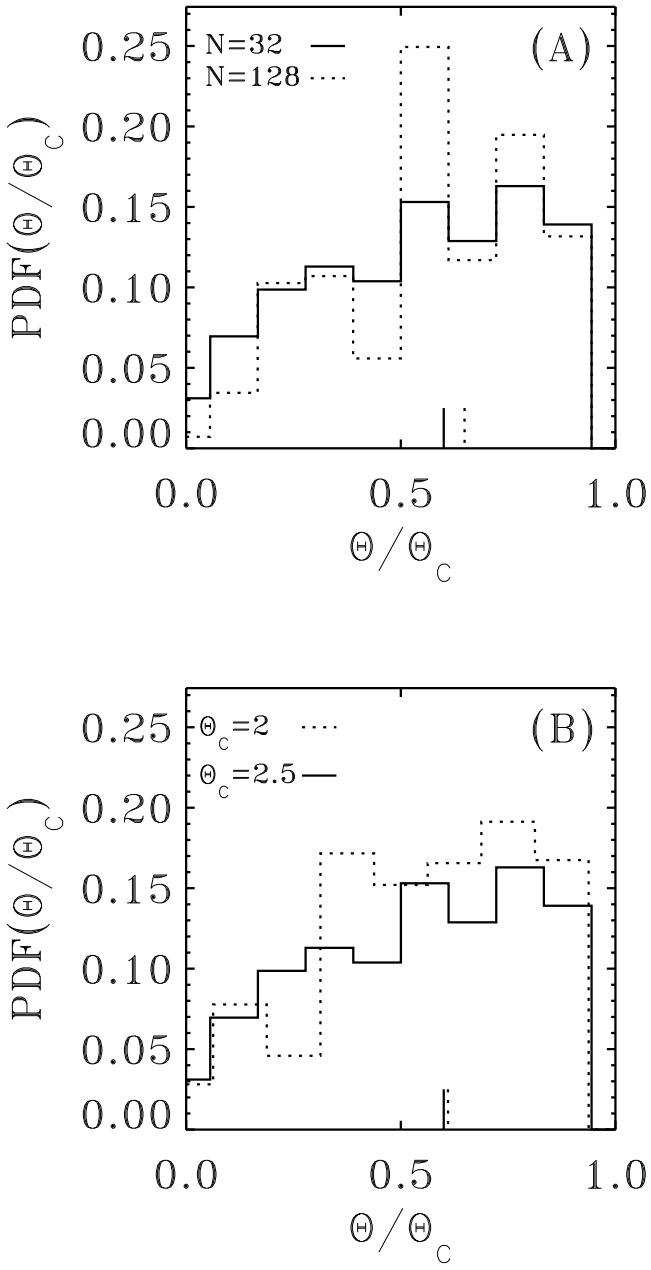

Fig. 5.— Distribution of angles (normalized to the critical threshold Θ_c. In (A) we compare simulations A1, A3 and in (B) we compare simulations A3 and C3 (see Table 1). Each distribution is constructed from a selection of forty non-avalanching iteration widely spaced in time but all in the SOC state. The vertical line segments along the abscissa are the means of the corresponding distributions.

do not necessarily lie at nearest neighbouring lattice sites.

The bottom panel on Fig. 6 shows the corresponding time series of energy release. Notice how the energy release can fluctuate quite markedly during the avalanche, with multiple sub-peaks presents; with real data, i.e., in the presence of a detection threshold, background noise or poor time resolution, it may be difficult to recognize this as a single avalanche, rather than a sequence of closely spaced smaller distinct avalanches. In other words, the energy release curve (corresponding conceptually to flare luminosity in hard radiation) is not comprised of a well-defined rising phase followed by a smooth decay phase, but is instead quite bursty. This feature is also present in time series of energy release in the LHMB model, but not to the same extent as here. Observations of flares in hard X-Rays are indeed far more bursty than at longer UV wavelengths (see, e.g., Fig. 2 in Warren & Warshall 2001).

3.4. Avalanche statistics

We now turn to the global characterization of avalanches, using the following four quantities: the peak energy release (P) is the maximum energy released in a single iteration in the course of an avalanche (such as at time C on the lower panel of Fig. 6); the total energy (E) is the sum of all energy released at all unstable sites in the course of an avalanche (the sum of all bins on the time series in Fig. 6); the duration (T) is the number of iterations from the onset of the avalanche to the recovery of stability across the whole lattice (between A and E on Fig. 6); and finally the waiting time (ΔT), the time elapsed between the end of one avalanche and the beginning of the following one. These quantities are thus readily extracted for each avalanche in the time series of energy release produced by the model. We can then build the probability distribution functions (hereafter PDF) for E, P, T and ΔT. The results of this exercise are shown in Figure 5 for model C3 (128×128 lattice with $\Theta_c = 2.5$). The PDFs for E, P and T all take the form of power-laws, i.e.:

$$\mathrm{PDF}(X) \propto X^{-\alpha_X} \ , \qquad X \in \{E, P, T\} \ , \tag{7}$$

spanning up to three orders of magnitude in size. The corresponding power law indices are listed in Table 2. For comparison, in the 2D scalar version of the LHMB model one finds $\alpha_E = 1.40$, $\alpha_P = 1.70$, $\alpha_T = 1.70$ for a 128×128 lattice (Charbonneau *et al.* 2001). Observational determinations, on the other hand, indicate $\alpha_E = 1.54 \pm 0.11$ (Aschwanden & Parnell 2002); α_P ranging from 1.79 ± 0.05 to 2.11 ± 0.13 (cf. Yashiro *et al.* 2006 and Veronig *et al.* 2002); the observational determination of α_T is usually the hardest, because of background noise and detection threshold effects, with values scattered in a broad range,

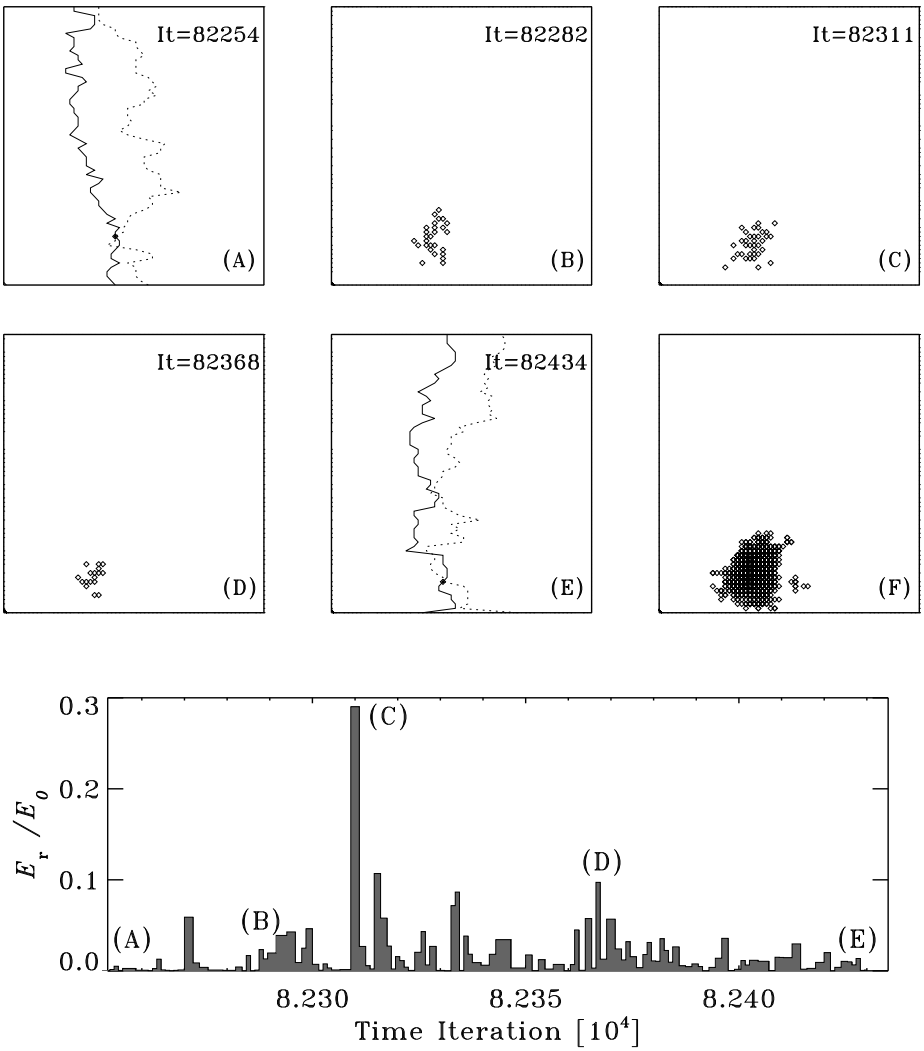

Fig. 6.— Snapshots of an ongoing avalanche in simulation B1 (A-E). (A) and (E) are the beginning and the end of the avalanche respectively. (B) and (D) are any two moments during the avalanche and (C) is extracted at the iteration of peak energy release during the avalanche. (F) shows the total area covered throughout the avalanche, i.e., the ensemble of lattice sites having gone unstable at least once during the avalanche. The bottom panel is the corresponding energy release time series; note that this does correspond to a single, continuous avalanche, energy release falling all the way back to zero only at the very end of the plotted time interval.

going from $\alpha_T \sim 1.15 \pm 0.04$ to 2.93 ± 0.12 (see Yashiro *et al.* 2006, Veronig *et al.* 2002, Yang *et al.* 2006 and Georgoulis *et al.* 2001). Our PDFs are thus slightly steeper than LHMB, but match observational statistics compararably well. The waiting time distribution, on the other hand, is exponential, reflecting the fact that the driving mechanism is a stationary, memoryless random process (in this context see Wheatland 2000 and Norman *et al.* 2001).

As can be seen on Figure 7, the avalanches size measures E, P and T are also statisticaly related via power law relationships of the general form

$$Y \propto X^{\gamma_{XY}} \ , \qquad X, Y \in \{E, P, T\} \ . \tag{8}$$

The associated power-law indices are again listed in Table 2. In the 2D scalar version of the LHMB model one finds: $\gamma_{PE} = 1.42$, $\gamma_{TE} = 1.72$, $\gamma_{TP} = 1.71$ for a 128×128 lattice (e.g., Charbonneau *et al.* 2001, Table II); observations suggest $\gamma_{PE} = 1.12 - 1.14$ and $\gamma_{TE} = 1.47 - 1.88$, $\gamma_{TP} = 1 - 1.64$ (Veronig *et al.* 2002; Georgoulis *et al.* 2001). Here the present avalanche model fits within the observationally determined ranges much better than the LHMB model.

One feature on Fig. 7A and B that has no counterpart in the Lu & Hamilton-type avalanche model is the presence of a well-wefined plateau in the PDFs for E and P, at the low end of the size distributions. Interestingly, no such plateau appears in the PDF for avalanche duration, suggesting that we are not witnessing here a break of finite size scaling. What is happening is that a small avalanche involving even just a single node can still liberate energy within a broad range, since this is determined by the difference in lengths squared before and after the reconnection for the two flux strands involved (cf. §2.2). Depending on the two strands being reconnected, this difference can span a wide range; yet if one of the nodes is displaced to an empty site in the course of redistribution (cf. §2.5), the avalanche immediately stops, leading to an avalanche of duration unity. Indeed, the statistics includes many avalanches for which $E = P$ (the signature of avalanches of duration unity) showing up as a well defined "diagonal" on Figure 8A. Moreover, moving on to Fig. 8B, avalanches of duration unity are seen to span five orders of magnitude in flare energy. Consequently, the upper left portions of Figure 8B and C are more populated than the corresponding correlation plots for the LHMB model (see Fig. 7 in LMHB, or Fig. 6 in Charbonneau *et al.* 2001), also leading to somewhat lower power law exponents in eqs. (8). However, we have not been able to come up with a simple, convincing explanation for the sharpness of the transition between the plateau and power-law portions of the total energy and peak PDFs.

Examination of Table 2 readily reveals that values of the α and γ exponents obtained on different lattice sizes or threshold angle all fit within each other within their error bars (associated with the least-squares fits). The existence of power-law relationships

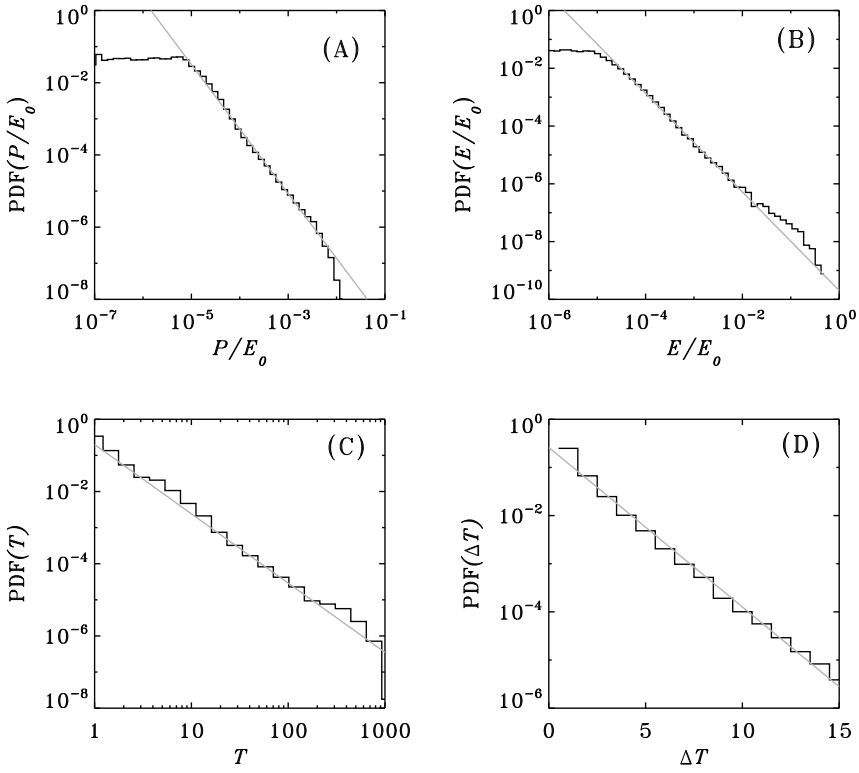

Fig. 7.— Probability distribution functions of avalanche size measures E, P and T and inter-event waiting time ΔT in a representative 1.5×10^6 iterations run of model C3. Only the portion of the time series corresponding to the SOC state is used to build these statistics.

Table 2: Simulations parameters and results

Simulation	α_E	α_P	α_T	γ_{PE}	γ_{TE}	γ_{TP}
A1	1.63 ± 0.03	1.79 ± 0.03	1.82 ± 0.09	1.13 ± 0.1	1.94 ± 0.3	1.45 ± 0.3
A2	1.63 ± 0.03	1.78 ± 0.02	1.95 ± 0.09	1.09 ± 0.1	1.73 ± 0.3	1.26 ± 0.25
A3	1.64 ± 0.04	1.73 ± 0.05	1.93 ± 0.05	1.09 ± 0.1	1.78 ± 0.3	1.34 ± 0.25
B1	1.70 ± 0.02	1.74 ± 0.03	1.80 ± 0.09	1.15 ± 0.1	1.75 ± 0.3	1.45 ± 0.25
B2	1.70 ± 0.03	1.76 ± 0.01	1.89 ± 0.09	1.23 ± 0.2	1.88 ± 0.2	1.32 ± 0.15
B3	1.65 ± 0.02	1.81 ± 0.02	1.90 ± 0.07	1.1 ± 0.2	1.60 ± 0.2	1.20 ± 0.2
C1	1.66 ± 0.05	1.84 ± 0.04	1.79 ± 0.08	1.26 ± 0.1	1.77 ± 0.2	1.20 ± 0.2
C2	1.72 ± 0.05	1.84 ± 0.04	1.85 ± 0.07	1.25 ± 0.2	1.80 ± 0.2	1.18 ± 0.2
C3	1.71 ± 0.05	1.78 ± 0.05	1.92 ± 0.02	1.20 ± 0.2	1.71 ± 0.2	1.15 ± 0.2

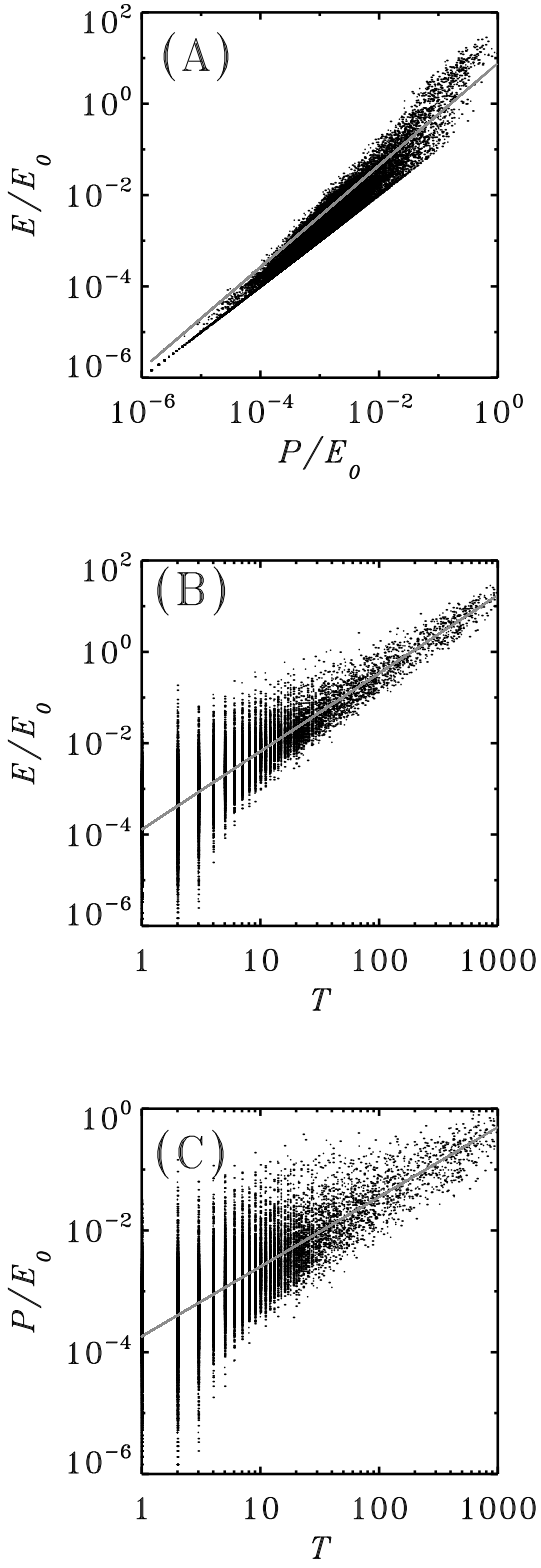

Fig. 8.— Correlation plots of avalanche energy (E) vs peak luminosity (P), energy vs duration (T) and peak luminosity vs duration, for simulation C3. Note that by definition, $E \geq P$. Gray lines are least-squares fits.

between avalanches size measures, together with the power-law form of their PDFs, and the constancy of the associated power-law exponents as the lattice size and threshold value are varied, all point to a lack of a typical scale for avalanches, a sine qua non feature of SOC systems.

4. Return to dimensionality

One of the most appealing differences between our SOC model for solar flares and the more conventional sandpile-like models is the possibility to restore physical dimensions to the simulations output. In what follows we outline how this can be achieved, reserving a fully detailed comparison to observations to a subsequent paper.

4.1. Loop size

Our cellular automaton is defined over a 2D unit lattice with equal horizontal and vertical spacing between lattice sites. If the lattice is to be interpreted as the outer surface of a coronal loop, with the horizontal (periodic) direction corresponding to the loop perimeter and the vertical to loop length, then one would expect the latter to be much larger than the former. In what follows we consider "typical" values for coronal loop lengths $L = 10^{10}\,\mathrm{cm}$ and diameter $D = 10^{8}\,\mathrm{cm}$, as listed in Golub & Pasachoff (1997). Note however that a 1:100 aspect ratio is probably too high if considering coronal loops at the small end of the observed size distribution (see Table 1 in Aschwanden *et al.* 2002b).

An important issue is the interpretation to be attached to an increase in lattice size; in going from a 32×32 to a 128×128 lattice (say), are we increasing fourfold the length and diameter of the loop —the *Ansatz* we favor at this juncture,— or are we implying that the loop is made of a greater number of finer strands that develop sharper kinks? Both interpretations are physically plausible, but have different consequences at the level of energetics. Recall (cf. Table 1) that for a fixed threshold angle Θ_c, the mean rate of energy release ($\langle\eta\rangle$), *expressed in terms of initial lattice energy*, falls with lattice size; under the first *Ansatz*, and for a fixed magnetic field strength doubling the lattice size increases the initial lattice energy fourfold, so that in fact larger lattices/loops liberate more energy in absolute terms. Under the second interpretation, a loop made up of many finer strands liberates less energy than a loop of the same size but made of fewer, thicker strands, and there is no dependency of the energy release rate on physical loop size; these features, in our opinion, add up to a less-than-satisfactory picture of energy release in coronal loops,

thus motivating our preference for the first interpretation.

4.2. Critical angle

Having ascribed linear dimensions to our pseudo-coronal loop, it becomes possible to translate the critical angle Θ_c on the unit lattice into a geometrical crossing angle between two strands of the coronal loop. For example, a critical threshold half-angle $\Theta_c/2 = 1.25\,\mathrm{rad}$ implies a horizontal-to-vertical internodal distance ratio of 3:1. With an assumed length-to-diameter ratio 100:1, and mapping the horizontal extent of the lattice onto the perimeter πD of a loop of diameter D, one finds a geometrically corrected critical angle $\Theta_c^* = 2\arctan(3\,\pi/100) \simeq 11°$, which is comparable to the 14° value estimated by Parker (1988), but notably smaller than the 40° value obtained in Dahlburg *et al.* 2005. Because we always increase lattice size by the same factor horizontally and vertically, increasing lattice size leaves this "physical" critical angle value unaltered. The key point here is mostly that, for a reasonable choice of length-to-diameter ratio, we recover a reasonable figure for the critical angle at which reconnection sets in, i.e., it is neither extremely small nor extremely large.

4.3. Energetics

With our adopted values for a typical coronal loop length and diameter, and an assumed field strength $B_0 = 200\,\mathrm{G}$ everywhere within the loop, one readily finds that in physical units our basic energy unit, the initial lattice energy is $E_0 \simeq 10^{29}\,\mathrm{erg}$. Examination of Figure 7B reveals that total flare energy covers the range $10^{-6} \leq E_r/E_0 \leq 0.9$, which then translates into energy covers the range $10^{23} \leq E_r \leq 10^{29}\,\mathrm{erg}$. The lower bound is not far removed from Parker's estimate or nanoflare energy. Note that larger flare energies can be produced on larger lattices, under our favored interpretation that increasing lattice size amounts to increasing loop size, and therefore the total magnetic energy content of the lattice. However, a detailed scaling analysis of flare energy release for varying loop sizes would also require specifications of the scaling relationship between physical loop parameters (magnetic field strength, etc) with linear size. Such scaling relationships have been inferred observationally (e.g. Aschwanden & Aschwanden, 2007), but at this juncture we opt to defer to a subsequent paper such detailed comparison with specific flare observations.

5. Concluding remarks

In this paper we presented and discussed a new avalanche model of magnetic energy release by solar flares, based on an idealized representation of a coronal loop. Our model is a line-based 2D cellular automaton, driven by stretching of randomly chosen line subsections. We identify these lines with strands of magnetic flux collectively making up the coronal loop. Stability is defined in terms of the angle subtended by two (or more) strands at lattice sites where they cross. Recovery to stability is enforced by cut-splice-move sequences mimicking magnetic reconnection, designed to lower lattice energy and alter topological linkage between strands.

Our simulations show that this driven dissipative cellular automaton evolves to a SOC state, with energy release occurring in a spatially and temporally intermittent fashion through avalanche of reconnection events collectively spanning a wide range of sizes, from a single site to large fraction of the whole lattice. The probability distribution functions for avalanche size measures (total energy released, peak luminosity, duration) take the form of power-laws, with indices comparing favorably to observationally-inferred values. In particular, our power law exponent for the PDF of total energy release, $\alpha_E = 1.66$, falls within the one-sigma range of the recent observational determination $\alpha_E = 1.52 - 1.77$ of Aschwanden & Parnell (2002), which takes into account some of the temperature-related observational biases affecting the analysis of EUV and soft-X-Ray flare data. This is a robust result that does not involve the tuning of any adjustable model parameter. The various avalanche size measures also correlate with each other as power laws, and here again our model compares favorably with observations, significantly better, in fact, than other SOC avalanche models of solar flares relying on "classical" sandpile-like isotropic lattices. Our results also show that the numerical values of these assorted power-law indices are independent of lattice size and stability threshold values. This is strongly suggestive of a self-organized critical state, although this remains to be rigorously proven by a formal scaling analysis (Morales & Charbonneau 2007, in preparation).

At the level of physical interpretation in the solar flare context, the model introduced herein offers a number of attractive features. First, the flux conservation constraint $\nabla \cdot \mathbf{B} = 0$ is satisfied by design; second, the avalanching process releases a significant fraction of the magnetic energy stored in the lattice; third, for reasonable values of coronal loop parameters (cf. §4), the energy released by avalanches in the model span the range from nanoflares ($\sim 10^{23}$ erg) to $\sim 10^{29}$ erg. Fourth, when mapped back onto a coronal loop of typical dimensions, the threshold angle above which reconnection sets in is of the same order of magnitude as the theoretical estimates of Parker (1988) and numerical simulations of Dahlburg *et al.* (2005). On the other hand, the logarithmic slope α_E of the probability

distribution function of energy release is too low for nanoflares to dominate the energy release budget. Therefore, although the present model is a viable model for the statistics of flare energy release, in its present form it does not represent a viable statistical model for coronal heating by nanoflares.

There exist a number of obvious extension to the avalanche model presented herein. Generalizing the model to three spatial dimensions would add "radial" structure to the pseudo-loop and, perhaps more importantly, allow the design of driving mechanism that would introduce a systematic sense of true twist within the lattice. At the level of comparison with observations, one particularly interesting avenue consists in mapping our pseudo-loop as a arching structure projected onto the plane of the sky, and investigate the statistical properties of projected avalanching areas. The probability distribution function of flaring areas is currently one of the major point of discrepancy between observations and LHMB-type avalanche models of solar flares (McIntosh *et al.*. 2002). It will also be interesting to make use of the various observationally inferred scaling laws between loop length, diameter, field strength, etc. (e.g., Aschwanden & Parnell 2002; Aschwanden & Aschwanden 2007), to investigate the flare/avalanche energy release budget in greater quantitative detail than the simple order-of-magnitude estimates presented in §4.

REFERENCES

Aschwanden, M. J. & Aschwanden, P. 2007, ApJ, preprint.

Aschwanden, M. J., Tarbell, T. D., Nightingale, R. W., Schrijver, C. J., Title, A., Kankelborg, C. C., Martens, P., & Warren, H. P. 2000, ApJ, 535, 1047

Aschwanden, M. J. & Parnell, C. 2002, ApJ, 572, 1048

Aschwanden, M. J., De Pontieu, B., Schrijver, C. J. & Title, A. M. 2002b, SolP, 206, 99

Bak, P., Tang, C., & Wiesenfeld, K. 1987, PRE, 59, 381

Bélanger, E., Vincent, A., & Charbonneau, P. 2007, SolP, in press.

Charbonneau, P., McIntosh, S. W., Liu, H.-L., & Bogdan, T. J. 2001, SolP, 203, 231

Dahlburg, R. B., Klimchuk, J. A., & Antiochos, S. K. 2005, ApJ, 622, 1191

Dennis, B. R. 1985, SolP, 100, 465

Georgoulis, M. K., Vilmer, N. & Crosby, N. B. 2001, A&A, 367, 326

Golub, L. & Pasachoff, J. M. 1997. The Solar Corona (Cambridge, UK: Cambridge University Press)

Isliker, H., Anastasiadis, A., & Vlahos, L. 2000, A&A, 363, 1134

Isliker, H., Anastasiadis, A., & Vlahos, L. 2001, A&A, 377, 1068

Isliker, H., Anastasiadis, A., Vassiliadis, D., & Vlahos, L. 1998, A&A, 335, 1085

Jensen, H. J. 1998, Self-organized criticality (Cambridge: Cambridge University Press)

Kadanoff, L. P., Nagel, S. R., Wu, L., & Zhou, S. 1989, PRA, 39, 6524

Klimchuk, J.A. 2006, SolP, 234, 41

Liu, H.-L., Charbonneau, P., Pouquet, A., Bogdan, T. J., & McIntosh, S. W. 2002, PRE, 66, 056111

Lu, E. T. 1995, PRL, 74, 2511

Lu, E. T., & Hamilton, R. J. 1991, ApJ, 380, L89 (LH91)

Lu, E. T., Hamilton, R. J., McTiernan, J. M., & Bromund, K. R. 1993, ApJ, 412, 841 (LHMB)

McIntosh, S. W., Charbonneau, P., Bogdan, T. J., Liu, H.-L., & Norman, J. P. 2002, PRE, 65, 046125

Norman, J. P., Charbonneau, P., McIntosh, S. W., and Liu, H.-L. 2001, ApJ, 557, 891

Parker, E. N. 1983, ApJ, 264, 642

Parker, E. N. 1988, ApJ, 330, 474

Parker, E. N. 1994, Spontaneus current sheets in magnetic Fields (Oxford University Press, New York)

Veronig, A., Temmer, M., Hanslmeier, A., Otruba, W. & Messerotti, M. 2002, A&A, 382, 1070

Warren, H. P. & Warshall, A. D. 2001, ApJ, 560, L87

Wheatland, M. S. 2000, ApJL, 536, L109

Yashiro, S., Akiyama, S., Gopalswamy, N. & Howard, R. A. 2006, ApJ, 650 (2), L143

Zirker, J. B. & Cleveland, F. M, 1993, SolP, 145, 119